FPGA-Based Continuous Control Set Model Predictive Current Control for PMSM System Using Multistep Error Tracking Technique

Fengxiang Wang, *Senior Member, IEEE*, Long He, *Member, IEEE*, and Jose Rodriguez, *Fellow Member, IEEE*

***Abstract*—To overcome the shortcomings of the conventional continuous control set model predictive current control (CCS-MPCC), such as large overshoot and poor robustness, an extended surface-mounted permanent magnet synchronous motor (SPMSM) model-based multistep error tracking CCS-MPCC (MSET-CCSMPCC) is proposed in this article. First, a traditional CCS-MPCC is derived based on the conventional SPMSM model and its robustness is analyzed by considering the parameter mismatches. Second, an extended SPMSM model is given by incorporating the lumped disturbances into one disturbance part. Third, a sliding mode differentiator improved fast terminal sliding mode disturbance observer is designed to track the disturbances. Fourth, by compensating the extended SPMSM model for the estimated *d*- and *q*-axes disturbances, an extended SPMSM model-based CCS-MPCC (EXM-CCSMPCC) is designed. However, the EXM-CCSMPCC has serious step response overshoot. Fifth, an extended SPMSM model-based single step error tracking CCS-MPCC is presented, whose dynamic response and steady-state performances deteriorate when the overshoot is reduced. Finally, an MSET-CCSMPCC is proposed to reduce the overshoot and improve the robustness while maintaining excellent dynamic and steady-state performances. Experiments are implemented on a field-programmable gate array based hardware system to verify the excellent performances of the proposed method.**

***Index Terms*—Fast terminal sliding mode disturbance observer (FTSMDO), model-based predictive current control (MPCC), multistep error tracking, permanent magnet synchronous machine (PMSM).**

I. Introduction

PERMANENT magnet synchronous motor (PMSM) has been widely employed in the industrial fields owning to its superior performances [1], [2]. Digitally controlled systems are required for high-performance PMSM operations, which largely prompt efficiency and precision. Field-oriented control (FOC) is one of the most popular digital control methods applied in the industry, which can independently control the torque and magnetizing flux [3].

In a classical FOC method, the inner current control loop determines the dynamic and steady-state performances of the stator current. In addition to the traditional proportional-integral (PI) control [4], many advanced current control methods have been proposed to improve the performances of the stator current, such as deadbeat-based predictive current control (DPCC) [5], [6], model-based predictive current control (MPCC) [7], [8], hysteresis current control [9], and so on. Among these methods, MPCC is one of the most popular strategies for current control, owing to its fast dynamic response and superior robustness [10]. The finite control set MPCC (FCS-MPCC) determines the optimal voltage vector by minimizing the predefined cost index [11]. Although an excellent transient performance is achieved, the FCS-MPCC causes large current and torque ripples. The continuous control set MPCC (CCS-MPCC), which is an important branch of MPCC, calculates the voltage reference by minimizing the predefined cost index [12]. The derived voltage reference is translated into switching signals by space vector pulsewidth modulation (SVPWM). Comparing with the FCS-MPCC, the CCS-MPCC causes smaller current ripples and requires fewer computation efforts [13]. However, conventional CCS-MPCC is sensitive to the parameter mismatches [14], which may induce steady-state error.

Surface-mounted PMSM (SPMSM) is a nonlinear and strong coupling control system where system parameter mismatches and external disturbances are inevitable, and deteriorate the performances of control algorithms. Disturbance observer (DO)-based control is one of the most effective antidisturbance methods [15]–[20]. Wang *et al.* [15] presented a finite-time DO to estimate the load disturbances. Combining with the nonsingular terminal sliding-mode control, an excellent disturbance rejection ability is acquired. A discrete Luenberger DO is designed to improve the robustness against parameter variations in [16], and as a result, a high-performance current control is achieved. Luenberger observer, which is a kind of linear observer, is widely used due to its intuitive structure. However, the Luenberger observer is sensitive to parameter variations, which results in inaccurate state estimation. To solve this problem, nonlinear DOs have received more and more attention. Sliding mode observer (SMO) is one of the most popular nonlinear observers, which is employed

Manuscript received June 25, 2019; revised November 22, 2019; accepted March 24, 2020. Date of publication April 1, 2020; date of current version July 31, 2020. This work was supported in part by the National Natural Science Funds of China under Grant 51877207, in part by the Science and Technology Program of Fujian Province under Grants 2019T3021 and 2018T3015, and in part by ANID through Projects FB0008, ACT192013, and 1170167. Recommended for publication by Associate Editor R. Kennel. *(Corresponding author: Long He.)*

Fengxiang Wang and Long He are with the Quanzhou Institute of Equipment Manufacturing, Haixi Institutes, Chinese Academy of Sciences, Jinjiang 362200, China (e-mail: fengxiang.wang@fjirsm.ac.cn; long.he@fjirsm.ac.cn).

Jose Rodriguez is with the Faculty of Engineering, Universidad Andres Bello, Santiago 8370146, Chile (e-mail: jose.rodriguez@unab.cl).

Color versions of one or more of the figures in this article are available online at https://ieeexplore.ieee.org.

Digital Object Identifier 10.1109/TPEL.2020.2984336

in a lot of high-performance SPMSM drives [17]–[20]. Lumped disturbances estimated by the SMO are fed forward to compensate the sliding mode controller in [17]. A lot of research works have been conducted on the well-known chattering problem in the traditional SMO, which may cause high-frequency dynamics [18]. Zhang *et al.* [19] proposed a sliding-mode reaching law, which reduces chatter while maintaining robust tracking performance. A unified high-order SMO (HSMO) has been designed in [20], which effectively reduces chatter.

In this article, an extended SPMSM model-based multistep error tracking CCS-MPCC (MSET-CCSMPCC) is proposed to reduce the overshoot of the current step response and improve the robustness of the conventional CCS-MPCC. An extended SPMSM model is given by incorporating the external disturbances and parameter variations into a disturbance part. To track the disturbance fast and accurately, a sliding mode differentiator (SMD) improved fast terminal sliding mode DO (FTSMDO) is designed. An extended SPMSM model-based CCS-MPCC (EXM-CCSMPCC) combining CCS-MPCC and FTSMDO is derived, which improves the robustness against lumped disturbances. The EXM-CCSMPCC exhibits high performances on dynamic response and steady state. However, there is an overshoot in the step response test, which limits its use. To solve the problem, an MSET-CCSMPCC is proposed finally, which reduces the overshoot while keeping excellent steady-state and dynamic response performances. Experiments were carried out on a field-programmable gate array (FPGA) based hardware system to verify the proposed methods.

The rest of the article is structured as follows. In Section II, a conventional CCS-MPCC is derived on the basis of the classical SPMSM model. In Section III, an extended SPMSM model is presented by considering the lumped disturbances, and an FTSMDO is designed to estimate the disturbance part of the model. Then, an extended SPMSM model-based CCS-MPCC (EXM-CCSMPCC) is proposed. To reduce the overshoot of the EXM-CCSMPCC in the step response test, a single step error tracking CCS-MPCC (SSET-CCSMPCC) is derived by assuming the error between the given current and feedback current to converge exponentially. Finally, an MSET-CCSMPCC is proposed to further improve the performances. In Section IV, experiments were carried out on an FPGA-based hardware system and the results are presented and analyzed. At last, the conclusion is drawn in Section V.

II. PMSM Model and Conventional CCS-MPCC

A. Modeling of the SPMSM

In a synchronous rotating frame, the current equations of an SPMSM can be denoted as [21]

$$\begin{cases} \dot{i}_d = \frac{1}{L}(u_d - Ri_d + Lp\omega_m i_q) \\ \dot{i}_q = \frac{1}{L}(u_q - Ri_q - Lp\omega_m i_d - \psi_r p\omega_m) \end{cases} \tag{1}$$

where u_d and u_q mean the stator voltages of the d- and q-axes, respectively, L is the stator inductance, R is the stator resistance, i_d and i_q are the stator currents of the d- and q-axes, respectively, ψ_r is the permanent magnet flux linkage, p is the number of pole pairs, and ω_m is the rotor angular velocity.

B. Conventional CCS-MPCC

According to Euler formula, (1) can be discretized as

$$\begin{cases} i_d(k+1) = i_d(k) + \frac{T_c}{L}(u_d(k) - Ri_d(k) \\ \qquad\qquad + Lp\omega_m(k)i_q(k)) \\ i_q(k+1) = i_q(k) + \frac{T_c}{L}(u_q(k) - Ri_q(k) \\ \qquad\qquad - Lp\omega_m(k)i_d(k) - \psi_r p\omega_m(k)) \end{cases} \tag{2}$$

where T_c is the current loop control period.

The cost index of the conventional CCS-MPCC is defined as

$$J(k) = (i_d^*(k) - i_d(k+1))^2 \tag{3}$$

$$+ \lambda(i_q^*(k) - i_q(k+1))^2 \tag{4}$$

where i_d^* is the d-axis current reference, i_q^* is the q-axis current reference, and λ is the weight coefficient. To optimize the control object, $J(k)$ in (3) is minimized by calculating appropriate voltage variables $u_d(k)$ and $u_q(k)$, which yields

$$\begin{cases} \frac{\partial J(k)}{\partial u_d(k)} = 0 \\ \frac{\partial J(k)}{\partial u_q(k)} = 0. \end{cases} \tag{5}$$

By solving the simultaneous (2), (3), and (5), the optimized voltage variables $u_d(k)$ and $u_q(k)$ are obtained

$$\begin{cases} u_d(k) = L\frac{i_d^*(k) - i_d(k)}{T_c} + Ri_d(k) - Lp\omega_m(k)i_q(k) \\ u_q(k) = L\frac{i_q^*(k) - i_q(k)}{T_c} + Ri_q(k) + Lp\omega_m(k)i_d(k) \\ \qquad + \psi_r p\omega_m(k). \end{cases} \tag{6}$$

C. Parameter Sensitivity Analysis

The parameters of the prediction model (2) include stator resistance, stator inductance, and permanent magnet flux linkage, which vary with the operating environment. The performance of the controller (6) would be deteriorated by the parameter variations and nonlinearity. Assume $R_v = R_n + R_\delta, L_v = L_n + L_\delta$, $\psi_{rv} = \psi_{rn} + \psi_{r\delta}$, where R_δ, L_δ, and $\psi_{r\delta}$ are the parameter variations, R_n, L_n, and ψ_{rn} are the real parameter values. Applying R_v, L_v, and ψ_{rv} to (6), it derives

$$\begin{cases} u_{d_\delta}(k) = L_n\frac{i_d^*(k) - i_d(k)}{T_c} + R_n i_d(k) \\ \qquad -L_n p\omega_m(k)i_q(k) + \Delta u_d(k) \\ u_{q_\delta}(k) = L_n\frac{i_q^*(k) - i_q(k)}{T_c} + R_n i_q(k) \\ \qquad +L_n p\omega_m(k)i_d(k) + \psi_{rn}p\omega_m(k) + \Delta u_q(k) \end{cases} \tag{7}$$

where $\Delta u_d(k) = L_\delta\frac{i_d^*(k) - i_d(k)}{T_c} + R_\delta i_d(k) - L_\delta p\omega_m(k)i_q(k)$, $\Delta u_q(k) = L_\delta\frac{i_q^*(k) - i_q(k)}{T_c} + R_\delta i_q(k) + L_\delta p\omega_m(k)i_d(k) + \psi_{r\delta}p\omega_m(k)$. Substituting (7) into (2), it derives

$$\begin{cases} i_d(k+1) = i_d^*(k) + \Delta u_d(k)\frac{T_c}{L_n} \\ i_q(k+1) = i_q^*(k) + \Delta u_q(k)\frac{T_c}{L_n}. \end{cases} \tag{8}$$

From (8), it can be found that errors between the reference currents and the feedback currents are induced by the parameter mismatches. In the following section, improved CCS-MPCC methods are proposed to track the currents accurately.

III. Extended SPMSM Model and Proposed CCS-MPCC

A. Extended SPMSM Model

The lumped disturbances of d- and q-axes can be regarded as $n_d = \frac{u_d}{L} - \frac{u_d^*}{L_N} - \frac{Ri_d}{L} + p\omega_m i_q$ and $n_q = \frac{u_q}{L} - \frac{u_q^*}{L_N} - \frac{Ri_q}{L} - p\omega_m i_d - \frac{\psi_r p\omega_m}{L}$, where L_N is the nominal stator inductance. The current equations of an SPMSM are denoted as

$$\begin{cases} \dot{i}_d = \frac{u_d^*}{L_N} + n_d \\ \dot{n}_d = a_d \end{cases} \tag{9}$$

$$\begin{cases} \dot{i}_q = \frac{u_q^*}{L_N} + n_q \\ \dot{n}_q = a_q \end{cases} \tag{10}$$

where u_d^* and u_q^* are the voltage references to d- and q-axes, respectively, a_d and a_q are the variation rates of the lumped disturbances.

B. Fast Terminal Sliding Mode DO Design

To track the lumped disturbances, an FTSMDO can be designed as

$$\begin{cases} \dot{\hat{i}}_d = \frac{u_d^*}{L_N} + \hat{n}_d + N_{d0} \\ \dot{\hat{n}}_d = N_{d1} \end{cases} \tag{11}$$

$$\begin{cases} \dot{\hat{i}}_q = \frac{u_q^*}{L_N} + \hat{n}_q + N_{q0} \\ \dot{\hat{n}}_q = N_{q1} \end{cases} \tag{12}$$

where $\hat{i}_d$, $\hat{i}_q$, $\hat{n}_d$, and $\hat{n}_q$ are the estimations of i_d, i_q, n_d, and n_q, respectively; and N_{d0}, N_{d1}, N_{q0}, N_{q1} are sliding mode control functions. By subtracting (9) to (11) and (10) to (12), the system error state equations are derived as

$$\begin{cases} \dot{e}_d = e_{nd} - N_{d0} \\ \dot{e}_{nd} = a_d - N_{d1} \end{cases} \tag{13}$$

$$\begin{cases} \dot{e}_q = e_{nq} - N_{q0} \\ \dot{e}_{nq} = a_q - N_{q1} \end{cases} \tag{14}$$

where $e_d = i_{d-\hat{i}_d}$, $e_{nd} = n_d - \hat{n}_d$, $e_q = i_{q-\hat{i}_q}$, and $e_{nq} = n_q - \hat{n}_q$.

To obtain finite-time convergence and good tracking accuracy, the FTSMDO surfaces are given as [22]

$$\begin{cases} s_d = \dot{e}_d + \alpha_d e_d + \beta_d |e_d|^{\gamma_d} \operatorname{sign}(e_d) = 0 \\ s_{nd} = \dot{e}_{nd} + \alpha_{nd} e_{nd} + \beta_{nd} |e_{nd}|^{\gamma_{nd}} \operatorname{sign}(e_{nd}) = 0 \end{cases} \tag{15}$$

$$\begin{cases} s_q = \dot{e}_q + \alpha_q e_q + \beta_q |e_q|^{\gamma_q} \operatorname{sign}(e_q) = 0 \\ s_{nq} = \dot{e}_{nq} + \alpha_{nq} e_{nq} + \beta_{nq} |e_{nq}|^{\gamma_{nq}} \operatorname{sign}(e_{nq}) = 0 \end{cases} \tag{16}$$

where $\alpha_d > 0$, $\beta_d > 0$, $0 < \gamma_d < 1$, $\alpha_{n_d} > 0$, $\beta_{n_d} > 0$, $0 < \gamma_{n_d} < 1$, $\alpha_q > 0$, $\beta_q > 0$, $0 < \gamma_q < 1$, $\alpha_{n_q} > 0$, $\beta_{n_q} > 0$, and $0 < \gamma_{n_q} < 1$.

Substituting (13) to (15) and (14) to (16), and considering e_{nd}, e_{nq}, a_d, and a_q as the disturbances of control functions, respectively, the FTSMDO control functions can be derived as

$$\begin{cases} N_{d0} = \alpha_d e_d + \beta_d |e_d|^{\gamma_d} \operatorname{sign}(e_d) \\ N_{d1} = \alpha_{nd} e_{nd} + \beta_{nd} |e_{nd}|^{\gamma_{nd}} \operatorname{sign}(e_{nd}) \end{cases} \tag{17}$$

$$\begin{cases} N_{q0} = \alpha_q e_q + \beta_q |e_q|^{\gamma_q} \operatorname{sign}(e_q) \\ N_{q1} = \alpha_{nq} e_{nq} + \beta_{nq} |e_{nq}|^{\gamma_{nq}} \operatorname{sign}(e_{nq}). \end{cases} \tag{18}$$

The d-axis FTSMDO is analyzed as follows, and the results are also applicable to the q-axis FTSMDO.

1) Stability of the Observer: A Lyapunov function is constructed as $V_d = \frac{1}{2} s_d^2$. Its time derivative is given as

$$\dot{V}_d = s_d \dot{s}_d. \tag{19}$$

Combining the first equations of (13), (15), and (17), the surface s_d can be derived as

$$s_d = e_{nd}. \tag{20}$$

According to (20) and the second equation of (13), the derivative of s_d with respect to time is

$$\dot{s}_d = a_d - N_{d1}. \tag{21}$$

Then, substituting (20) and (21) to (19), $\dot{V}_d$ can be calculated as

$$\dot{V}_d = a_d s_d - N_{d1} s_d. \tag{22}$$

Substitute the second equation of (17) to (22), and the $\dot{V}_d$ can be derived as

$$\begin{aligned} \dot{V}_d &= a_d s_d - (\alpha_{nd} s_d^2 + \beta_{nd} |s_d|^{\gamma_{nd}} |s_d|) \\ &\le |s_d| (|a_d| - \alpha_{nd} |s_d| - \beta_{nd} |s_d|^{\gamma_{nd}}). \end{aligned} \tag{23}$$

Therefore, when $|a_d| < \alpha_{nd}|s_d| + \beta_{nd}|s_d|^{\gamma_{nd}}$, it obtains $\dot{V}_d < 0$ ($s_d \neq 0$). Considering the control period of the current loop is so short that a_d can be regarded as zero, $\dot{V}_d < 0$ ($s_d \neq 0$) is drawn when $\alpha_{nd} > 0$ and $\beta_{nd} > 0$. Thus, according to the Lyapunov stability theorem, the FTSMDO surface is reached in a finite time and stay on it thereafter. The following equation is obtained accordingly

$$\dot{e}_d = -\alpha_d e_d - \beta_d |e_d|^{\gamma_d} \operatorname{sign}(e_d). \tag{24}$$

Assuming the initial e_d does not stay at zero and the γ_d is well chosen, $e_d = 0$ can be reached in a finite time. According to (24), the physical interpretation can be depicted as follows.

1) If e_d stays far away from zero, it obtains $\dot{e}_d \approx -\alpha_d e_d$, which means the e_d converges exponentially.
2) If e_d stays close to zero, it obtains $\dot{e}_d \approx -\beta_d |e_d|^{\gamma_d} \operatorname{sign}(e_d)$, which becomes a terminal attractor.

By substituting $e_d = 0$ into (24), it obtains $e_d = \dot{e}_d = 0$, which means the designed FTSMDO has the properties of the HSMO [23]. From (20), e_{nd} vanishes to zero with time as well as s_d.

2) Reaching time of e_d: By solving (24), the precise time to arrive at $e_d = 0$ can be derived as

$$t_d = \frac{1}{\alpha_d (1 - \gamma_d)} \ln \frac{\alpha_d |e_d(0)|^{1-\gamma_d} + \beta_d}{\beta_d}. \tag{25}$$

3) Calculation of $\dot{e}_d$: Let $\dot{e}_d = x$. In common, x is calculated as $x \approx \frac{1}{T_c}(e_d(k) - e_d(k-1))$, which is sensitive to the noise [24]. To improve the quality of $\dot{e}_d$, an exponential reaching law based SMD is given as follows [25]:

$$\begin{cases} \dot{\hat{e}}_d = \hat{x} - l_{d0} \operatorname{sign}(\hat{e}_d - e_d) - l_{d1}(\hat{e}_d - e_d) \\ \dot{\hat{x}} \ = -l_{d2} \operatorname{sign}(\hat{e}_d - e_d) - l_{d3}(\hat{e}_d - e_d) \end{cases} \tag{26}$$

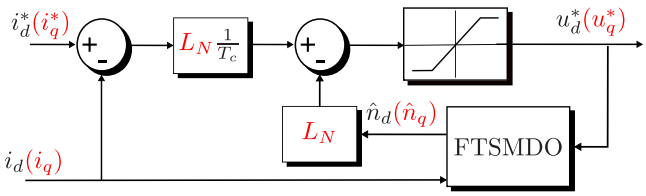

Fig. 1. Block diagram of the EXM-CCSMPCC.

where $\hat{e}_d$ is the estimated value of e_d, $\hat{x}$ is the derivative of $\hat{e}_d$, which derives $x \approx \hat{x}$, $l_{d0} > 0$, $l_{d1} > 0$, $l_{d2} > 0$, $l_{d3} > 0$.

C. Extended SPMSM Model-Based CCS-MPCC

Substitute the estimated $\hat{n}_d$, $\hat{n}_q$ to the extended SPMSM model, and it can be rewritten as

$$\begin{cases} \dot{i}_d = \frac{u_d^*}{L_N} + \hat{n}_d \\ \dot{i}_q = \frac{u_q^*}{L_N} + \hat{n}_q \end{cases} \tag{27}$$

Equation (27) can be discretized as

$$\begin{cases} i_d(k+1) = i_d(k) + T_c(\frac{u_d^*(k)}{L_N} + \hat{n}_d(k)) \\ i_q(k+1) = i_q(k) + T_c(\frac{u_q^*(k)}{L_N} + \hat{n}_q(k)). \end{cases} \tag{28}$$

The cost index of the EXM-CCSMPCC is defined as

$$\begin{aligned} J_e(k) = &(i_d^*(k) - i_d(k+1))^2 \\ &+ \lambda(i_q^*(k) - i_q(k+1))^2. \end{aligned} \tag{29}$$

The cost index $J_e(k)$ in (29) is minimized by calculating appropriate voltage variables $u_d^*(k)$ and $u_q^*(k)$, which yields

$$\begin{cases} \frac{\partial J_e(k)}{\partial u_d^*(k)} = 0 \\ \frac{\partial J_e(k)}{\partial u_q^*(k)} = 0. \end{cases} \tag{30}$$

By solving the simultaneous (28), (29), and (30), the optimized voltage variables $u_d^*(k)$ and $u_q^*(k)$ are derived as

$$\begin{cases} u_d^*(k) &= L_N\frac{i_d^*(k) - i_d(k)}{T_c} - L_N\hat{n}_d(k) \\ u_q^*(k) &= L_N\frac{i_q^*(k) - i_q(k)}{T_c} - L_N\hat{n}_q(k). \end{cases} \tag{31}$$

Fig. 1 shows the diagram of the EXM-CCSMPCC and the flowchart of the EXM-CCSMPCC is shown in Fig. 5(a). The cost index of the proposed EXM-CCSMPCC is constructed to achieve the fastest tracking, and as a result, the i_d and i_q track the i_d^* and i_q^* as fast as possible. However, serious overshoot occurs in the step response test by using the EXM-CCSMPCC. To eliminate the overshoot, a new cost index is constructed in the next section.

1) Stability of the EXM-CCSMPCC: A lyapunov function is constructed as (32) to prove that the $e_{id} = i_d^* - i_d$ and $e_{iq} = i_q^* - i_q$ vanish with time when the current controller (31) is applied

$$\begin{cases} V_{id} &= \frac{1}{2}e_{id}^2 \\ V_{iq} &= \frac{1}{2}e_{iq}^2. \end{cases} \tag{32}$$

Derivations of the V_{id} and V_{iq} are calculated as

$$\begin{cases} \frac{dV_{id}}{dt} = -e_{id}(\frac{u_d^*}{L_N} + n_d) = -\frac{e_{id}^2}{T_c} - e_{id}e_{nd} \\ \frac{dV_{iq}}{dt} = -e_{iq}(\frac{u_q^*}{L_N} + n_q) = -\frac{e_{iq}^2}{T_c} - e_{iq}e_{nq} \end{cases} \tag{33}$$

where the e_{nd} and e_{nq} decrease over time when the FTSMDOs are applied. Therefore, the e_{id} and e_{iq} vanish with time.

D. Extended SPMSM Model-Based Single Step Error Tracking CCS-MPCC

Let

$$\begin{cases} \Delta_d = i_d^* - i_d \\ \Delta_q = i_q^* - i_q. \end{cases} \tag{34}$$

Assume the errors between the given currents and the predicted currents converge exponentially, namely, $\Delta_d = e^{-\rho t}$, $\Delta_q = e^{-\rho t}$. The time derivatives of Δ_d and Δ_q can be derived as

$$\begin{cases} \dot{\Delta}_d = -\rho\Delta_d \\ \dot{\Delta}_q = -\rho\Delta_q. \end{cases} \tag{35}$$

Let $\eta = (1 - T_c\rho)$, and (35) can be discretized as

$$\begin{cases} \Delta_d(k+1) = \eta\Delta_d(k) \\ \Delta_q(k+1) = \eta\Delta_q(k) \end{cases} \tag{36}$$

where $0 < \eta < 1$.

Therefore, the cost index of the SSET-CCSMPCC is designed as

$$\begin{aligned} J_\Delta(k) = &\lambda_{d0}(\Delta_d(k)\eta - \Delta_d(k+1))^2 \\ &+ \lambda_{q0}(\Delta_q(k)\eta - \Delta_q(k+1))^2. \end{aligned} \tag{37}$$

If the cost function $J_\Delta(k)$ in (37) is minimized, (35) is approximately satisfied. Thus, the Δ_d and Δ_q converge exponentially.

According to (34), it obtains

$$\begin{cases} \Delta_d(k) = i_d^*(k-1) - i_d(k) \\ \Delta_q(k) = i_q^*(k-1) - i_q(k) \\ \Delta_d(k+1) = i_d^*(k) - i_d(k+1) \\ \Delta_q(k+1) = i_q^*(k) - i_q(k+1). \end{cases} \tag{38}$$

Substituting (28) and (38) into (37), and solving $\frac{\partial J_\Delta(k)}{\partial u_d^*(k)} = 0$, $\frac{\partial J_\Delta(k)}{\partial u_q^*(k)} = 0$, it obtains

$$\begin{cases} u_d^*(k) = \frac{L_N}{T_c}(i_d^*(k) - \eta i_d^*(k-1) \\ \qquad -(1-\eta)i_d(k) - T_c\hat{n}_d(k)) \\ u_q^*(k) = \frac{L_N}{T_c}(i_q^*(k) - \eta i_q^*(k-1) \\ \qquad -(1-\eta)i_q(k) - T_c\hat{n}_q(k)). \end{cases} \tag{39}$$

Fig. 2 shows the block diagram of the SSET-CCSMPCC, where z indicates that one sampling period delay is applied, and the flowchart of the SSET-CCSMPCC is shown in Fig. 5(b). In the step response test, large η will eliminate the overshoots of the i_d and i_q, but increase the tracking time and the current ripples. To solve the problem, an MSET-CCSMPCC is proposed in the next section.

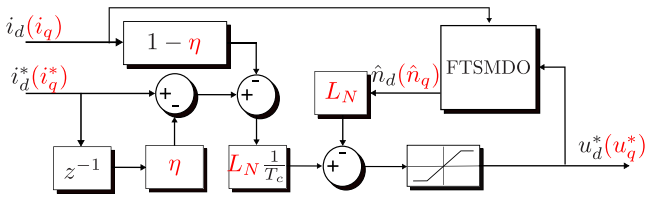

Fig. 2. Block diagram of the SSET-CCSMPCC.

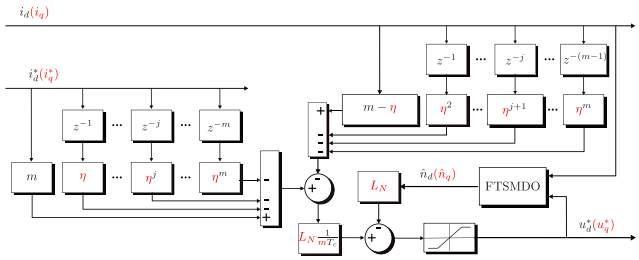

Fig. 3. Block diagram of the MSET-CCSMPCC.

E. Extended SPMSM Model-Based Multistep Error Tracking CCS-MPCC

According to (36), it derives

$$\begin{cases} \Delta_d(k+1) = \eta^{j+1}\Delta_d(k-j) \\ \Delta_q(k+1) = \eta^{j+1}\Delta_q(k-j). \end{cases} \tag{40}$$

The cost index of the MSET-CCSMPCC can be constructed as follows:

$$J_{M_\Delta}(k) = \sum_{j=0}^{m-1} \lambda_{dj}(\Delta_d(k-j)\eta^{j+1} - \Delta_d(k+1))^2 + \sum_{j=0}^{m-1} \lambda_{qj}(\Delta_q(k-j)\eta^{j+1} - \Delta_q(k+1))^2 \tag{41}$$

where $\Delta_d(k-j) = i_d^*(k-j-1) - i_d(k-j)$, $\Delta_q(k-j) = i_q^*(k-j-1) - i_q(k-j)$, and $\Delta_d(k+1)$, $\Delta_q(k+1)$ can be derived by combining (28) and (38). Assuming that each subitem has the same weight, λ_{dj} and λ_{qj} can be chosen as 1. By solving $\frac{\partial J_{M_\Delta(k)}}{\partial u_d^*(k)} = 0$ and $\frac{\partial J_{M_\Delta(k)}}{\partial u_q^*(k)} = 0$, the cost index $J_{M_\Delta(k)}$ in (41) is minimized, and the appropriate voltage variables $u_d^*(k)$ and $u_q^*(k)$ can be calculated as

$$\begin{cases} u_d^*(k) = \frac{L_N}{mT_c}(mi_d^*(k) - \sum_{j=0}^{m-1}\eta^{j+1}i_d^*(k-j-1) \\ \qquad -(mi_d(k) - \sum_{j=0}^{m-1}\eta^{j+1}i_d(k-j)) - mT_c\hat{n}_d(k)) \\ u_q^*(k) = \frac{L_N}{mT_c}(mi_q^*(k) - \sum_{j=0}^{m-1}\eta^{j+1}i_q^*(k-j-1) \\ \qquad -(mi_q(k) - \sum_{j=0}^{m-1}\eta^{j+1}i_q(k-j)) - mT_c\hat{n}_q(k)). \end{cases} \tag{42}$$

In Fig. 3, the block diagram of the MSET-CCSMPCC is depicted. The flowchart of the MSET-CCSMPCC is shown in Fig. 5.

1) Stability of the MSET-CCSMPCC: As the current loop control period T_c is sufficiently small, the MSET-CCSMPCC can be expressed in s-domain as

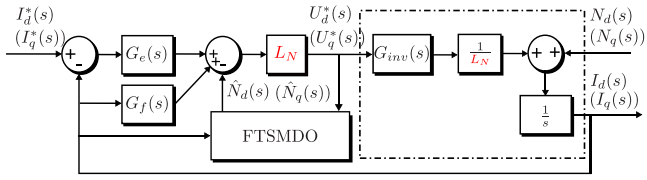

Fig. 4. Block diagram of the MSET-CCSMPCC in s-domain.

$$\begin{cases} U_d^*(s) = L_N(G_e(s)(I_d^*(s) - I_d(s)) + G_f(s)I_d(s) - \hat{N}_d(s)) \\ U_q^*(s) = L_N(G_e(s)(I_q^*(s) - I_q(s)) + G_f(s)I_q(s) - \hat{N}_q(s)) \end{cases} \tag{43}$$

where $G_e(s) = \frac{1}{mT_c}(m - \frac{\eta(1-(\eta^m(1+mT_cs)^{-1}))}{1+T_cs-\eta})$, $G_f(s) = \frac{s}{m}\frac{\eta(1-(\eta^m(1+mT_cs)^{-1}))}{1+T_cs-\eta}$. Fig. 4 shows the block diagram of the MSET-CCSMPCC in s-domain, where $G_{\text{inv}}(s) = \frac{1}{T_cs+1}$ is the transfer function of the SVPWM-based inverter. The closed-loop transfer function can be derived as

$$\begin{cases} I_d(s) = \frac{G_{in}(s)}{G_d(s)}I_d^*(s) - \frac{G_{nn}(s)(G_{inv}(s)\hat{N}_d(s) - N_d(s))}{G_d(s)} \\ I_q(s) = \frac{G_{in}(s)}{G_d(s)}I_q^*(s) - \frac{G_{nn}(s)(G_{inv}(s)\hat{N}_q(s) - N_q(s))}{G_d(s)}. \end{cases} \tag{44}$$

Ignoring high-order items of T_c, which is sufficiently small, it derives

$$\begin{cases} G_{in}(s) = (1-\eta)(T_cm(1+m)s + (\sum_{j=1}^{m}(1-\eta^j))) \\ G_d(s) = (1-\eta)(m^2 + (\sum_{j=1}^{m}(2-\eta^j)))T_cs \\ \qquad + (1-\eta)(\sum_{j=1}^{m}(1-\eta^j)) \\ G_{nn}(s) = -T_cm(\eta-1). \end{cases} \tag{45}$$

Letting $G_d(s) = 0$, the characteristic root lies in the left half-plane, and the control system is stable. Assuming $s = 0$, it derives

$$\begin{cases} I_d(s) = I_d^*(s) + \frac{(-T_cm(\eta-1))E_{nd}(s)}{m-\eta-\eta m+\eta\eta^m} \\ I_q(s) = I_q^*(s) + \frac{(-T_cm(\eta-1))E_{nq}(s)}{m-\eta-\eta m+\eta\eta^m} \end{cases} \tag{46}$$

where $E_{nd}(s)$ and $E_{nq}(s)$ converge to zero when the FTSMDOs are applied. Thus, the i_d and i_q can precisely track the i_d^* and i_q^*, respectively, in the steady state.

IV. Experimental Results

An FPGA-based hardware system has been designed as shown in Fig. 6. The XC7Z020-CLG484-1, which incorporates dual-core Cortex-A9 processors and an FPGA core, was utilized as the control unit. A PWM Generator, an analog-to-digital converter (ADC) interface, an Encoder Decoding are implemented on the FPGA core by employing Verilog language. By properly designing the PWM Generator module clock, a desired resolution is achieved. A parallel interface is designed to interface to a 16-bit, simultaneous sampling ADC AD7606. The Encoder Decoding is designed to interface to an incremental encoder, which provides information on the sensor's current position and the period between two encoder events. CPU0 (CPU: central processing unit), which runs an embedded Linux, communicates

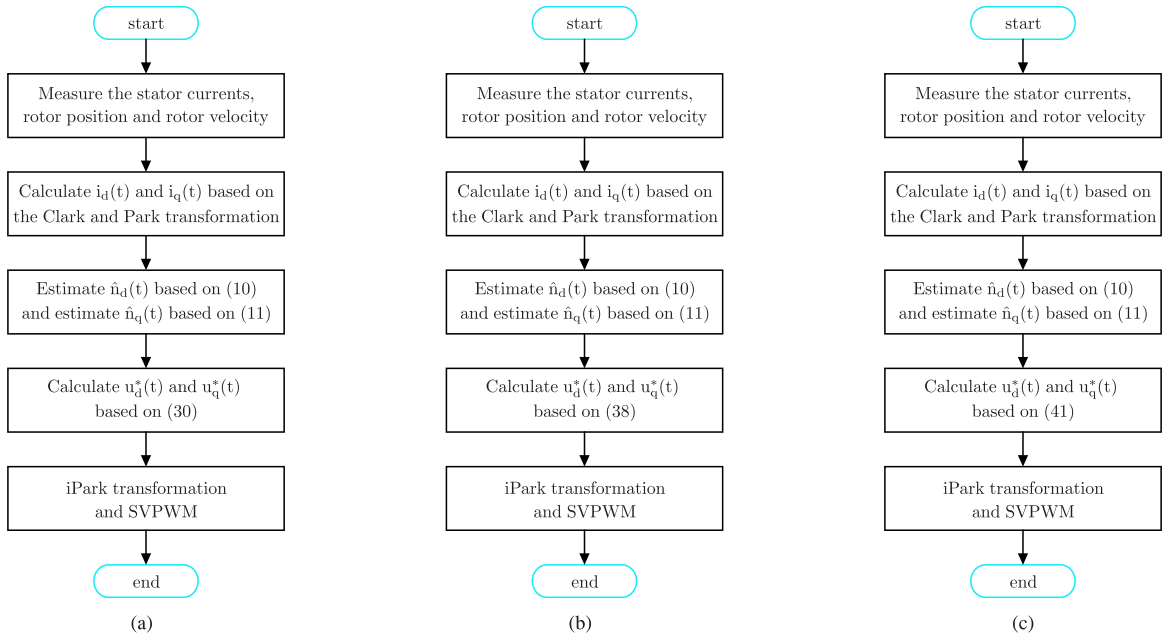

Fig. 5. Flow diagrams of the proposed methods. (a) Flow diagram of EXM-CCSMPCC. (b) Flow diagram of SSET-CCSMPCC. (c) Flow diagram of MSET-CCSMPCC.

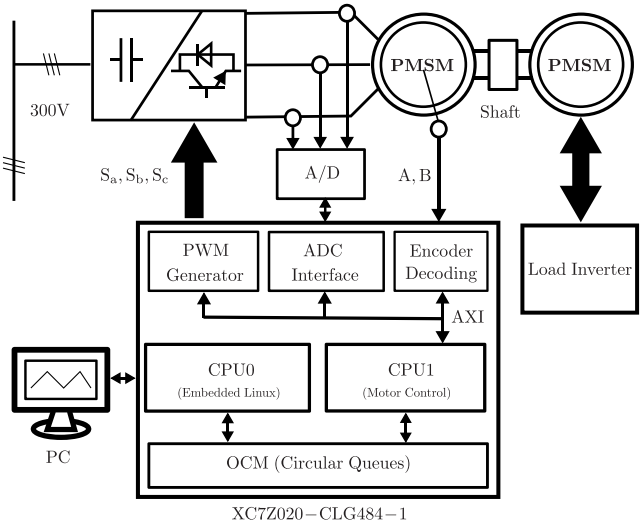

Fig. 6. Block diagram of the designed FPGA-based hardware system.

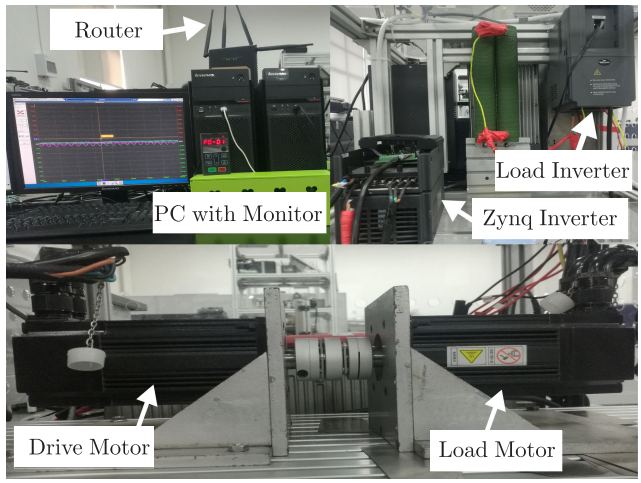

Fig. 7. Experimental setup description.

with a control and monitoring software installed on the computer via Ethernet. The motor control algorithms are implemented on the CPU1, which communicates with the CPU0 via the on-chip memory.

To verify the proposed algorithms, an SPMSM test bench has been established as shown in Fig. 7. Two SPMSMs manufactured by Wenling Yuhai Electromechanical Corporation with the parameters specified in Table I are coupled via a flexible coupling. The drive motor, which is driven by an FPGA-based hardware system, is used to test the algorithms. The load motor, which is driven by a 3.0 kW commercial inverter made by Micno Corporation, is applied to provide the speed. An incremental encoder with a resolution of 2500 pulses per revolution (P/R) is utilized for measuring the SPMSM speed. Three high-precision sampling resistors are used to measure the stator currents.

In the following sections, experimental results are presented and analyzed. In part A, the proposed methods are tested to verify the effectiveness. In part B, the performances of the designed FTSMDO are verified. In parts C and D, the proposed methods are explicitly compared with the existed conventional CCS-MPCC for sharing the advantages and drawbacks.

A. *Speed Reversal Performance*

Experiments to validate the performances of the EXM-CCSMPC and MSET-CCSMPCC during the rated full-speed

TABLE I
PARAMETERS OF SPMSM

Descriptions	Parameters	Nominal Values
Stator resistance	R	$1.7912\,\Omega$
Stator inductance	L_N	$3.5\,\mathrm{mH}$
Pole pairs	p	4
PM flux	ψ_r	$0.0799\,\mathrm{Vs}$
Rated power	P_N	$0.75\,\mathrm{kW}$
Rotor inertia	J_n	$0.00024\,\mathrm{Kg}\cdot\mathrm{m}^2$
Rated current	I_N (eff.)	$3.5\,\mathrm{A}$
Rated speed	ω_{MN}	$3000\,\mathrm{rpm}$
Rated voltage	U_N (eff.)	$220\,\mathrm{V}$
Rated torque	T_{MN}	$2.4\,\mathrm{Nm}$
DC link voltage	V_{dc}	$300\,\mathrm{V}$

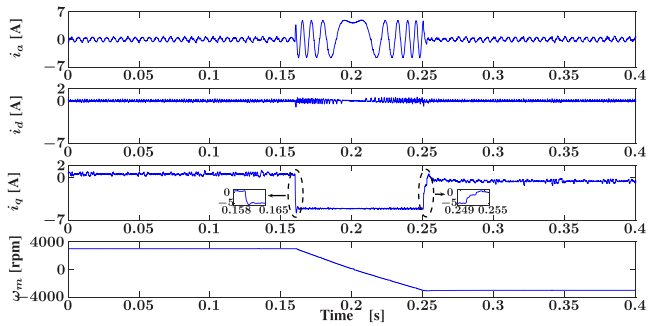

Fig. 8. Experimental results during the rated full-speed reversal process. (PI cascade with EXM-CCSMPC, from 3000 to −3000 r/min).

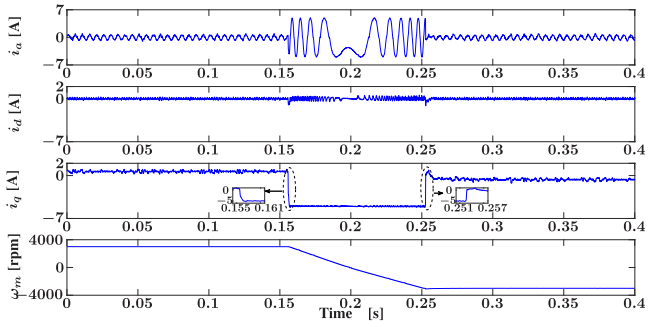

Fig. 9. Experimental results during the rated full-speed reversal process. (PI cascade with MSET-CCSMPCC, from 3000 to −3000 r/min).

range are carried out, respectively, in Figs. 8 and 9, where the load motor is out of service and the ω_m^* is directly changed in the program. In both experiments, the PI control with the same parameters is applied to the outer speed loop, and the given speed ω_m^* is changed from 3000 to −3000 r/min at 0.16 s. The q-axis currents of both methods jump to their upper bounds within 3 ms, but the i_q overshoot of the MSET-CCSMPCC (almost no overshoot) is much smaller than that of the EXM-CCSMPC (0.8 A

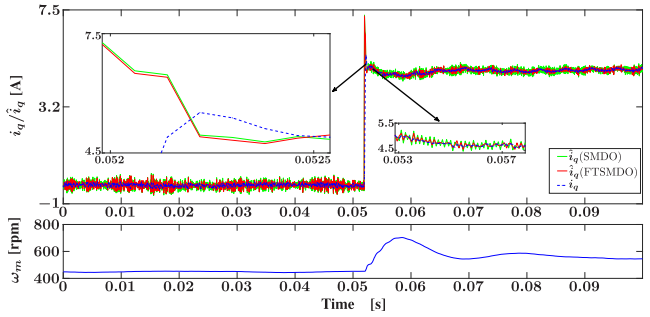

Fig. 10. $\hat{i}_q$ experimental results of the FTSMDO and SMDO under the i_q step response test with the conventional CCS-MPCC. (450 r/min, i_q alters from 0 to 5 A).

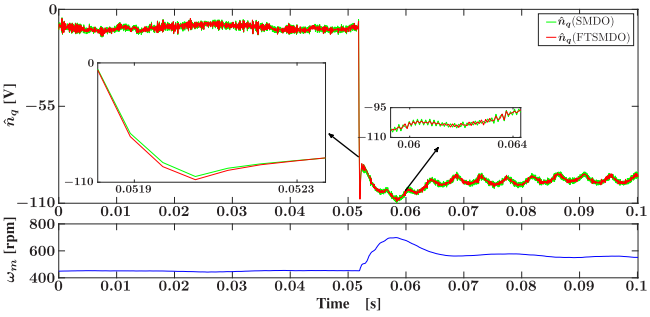

Fig. 11. $\hat{n}_q$ experimental results of the FTSMDO and SMDO under the i_q step response test with the conventional MPCC. (450 r/min, i_q alters from 0 to 5 A).

overshoot). As i_q is proportional to the electromagnetic torque, the drive SPMSM reverses from 3000 to −3000 r/min fast in both experiments (within 0.09 s). The experimental results indicate that the proposed EXM-CCSMPCC and MSET-CCSMPCC have the fast dynamic response in the full-speed range. However, the MSET-CCSMPCC has better performance considering the overshoot suppression.

B. Performance of the FTSMDO

To verify the excellent performances of the designed FTSMDO, an exponential reaching law based SMDO is given below as a comparison method

$$\begin{cases} \dot{\hat{i}}_q &= \frac{u_q^*}{L_N} + \hat{n}_q + \alpha_q e_q + \beta_q \mathrm{sign}(e_q) \\ \dot{\hat{n}}_q &= \alpha_{nq}(\alpha_q e_q + \beta_q \mathrm{sign}(e_q)) \end{cases} \tag{47}$$

where the parameters α_q, β_q, and α_{nq} are chosen to be of the same values as that of FTSMDO.

Experiments to validate the performances of the SMDO and FTSMDO during the i_q step response test are carried out in Figs. 10 and 11, where the i_q^* is directly changed in the program and the motor speed is provided by the Micno commercial inverter. The conventional CCS-MPCC is applied to the current loop of the FPGA-based hardware system, and the i_q and u_q^* are fed back to the SMDO and FTSMDO, respectively. The drive motor runs at 450 r/min, and the i_q^* is changed from 0 to 5 A. It can be seen that the FTSMDO tracks slightly faster than the

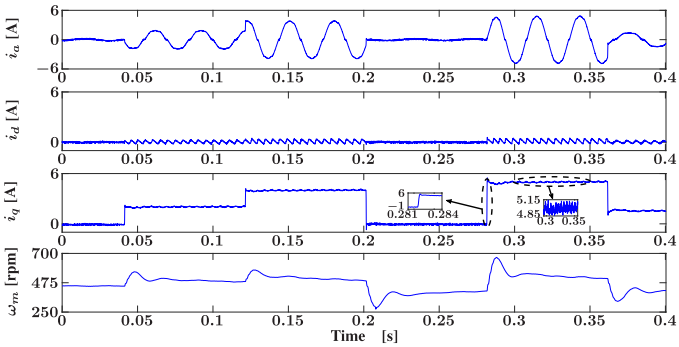

Fig. 12. Experimental results of the i_q step response test. (With the conventional CCS-MPCC, 450 r/min).

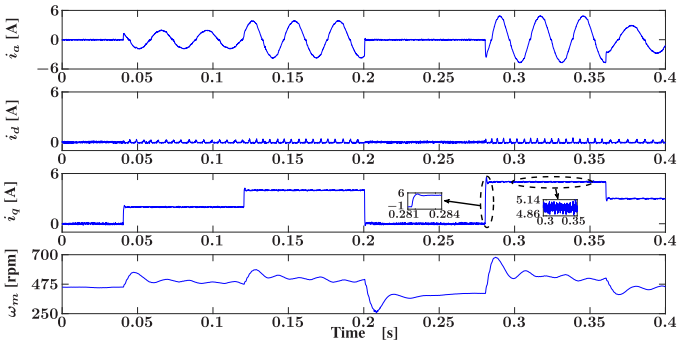

Fig. 13. Experimental results of the i_q step response test. (With the EXM-CCSMPCC, 450 r/min).

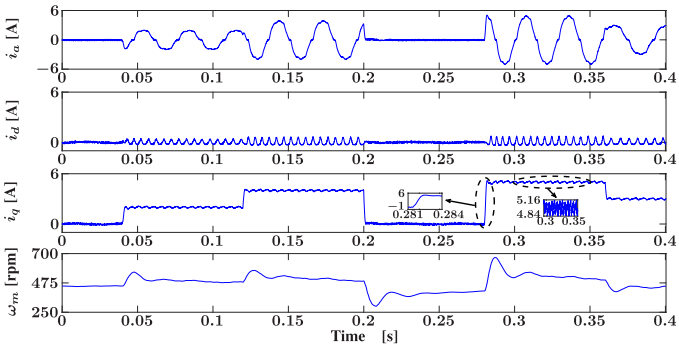

Fig. 14. Experimental results of the i_q step response test. (With the SSET-CCSMPCC, 450 r/min).

SMDO, and the $\hat{n}_q$ and $\hat{i}_q$ of the SMDO have more serious chatter than that of the FTSMDO (approximately two times larger).

C. I_q Step Response Performance

The i_q step response performances of the conventional CCS-MPCC, EXM-CCSMPCC, SSET-CCSMPCC, and MSET-CCSMPCC are evaluated in Figs. 12, 13, 14, and 15, respectively, where the i_q^* is directly changed in the program and the motor speed is provided by the Micno commercial inverter. It can be seen that both the conventional CCS-MPCC and EXM-CCSMPCC have serious overshoots (0.8 A in the 0–5 A step

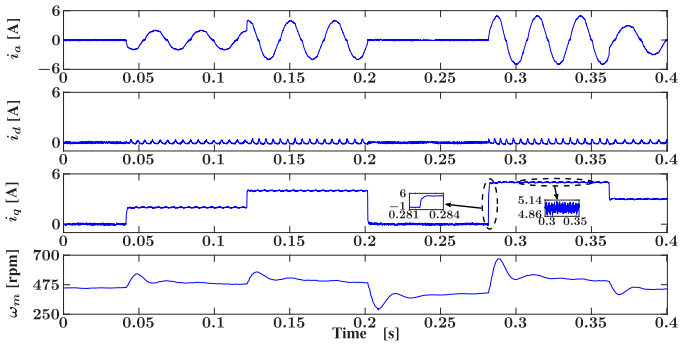

Fig. 15. Experimental results of the i_q step response test. (With the MSET-CCSMPCC, 450 r/min).

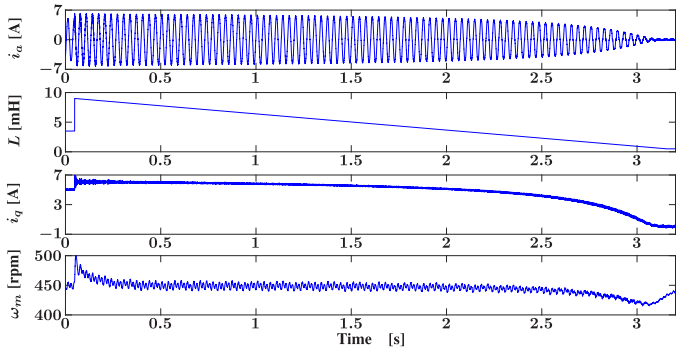

Fig. 16. Steady-state performance under the stator inductance variation. (With the conventional CCS-MPCC, 450 r/min, 5 A i_q).

response test). The overshoots of the i_q are eliminated with the proposed SSET-CCSMPCC and MSET-CCSMPCC methods in the 0–2, 2–4, 4–0, and 0–5 A step response tests. However, the SSET-CCSMPCC tracks more slowly (2 ms approximately) than three other methods (within 1 ms). The proposed EXM-CCSMPCC and MSET-CCSMPCC have comparable steady-state performances and the current variations are smaller than 0.28 A when the i_q operates at 5 A. The current variations of the SSET-CCSMPCC (0.32 A when the i_q operates at 5 A) and the conventional CCS-MPCC (0.3 A when the i_q operates at 5 A) are larger than those of two other methods.

D. Parameter Sensitivity Evaluation

From (31) and (42), the proposed EXM-CCSMPCC and MSET-CCSMPCC are only affected by the stator inductance, while the conventional CCS-MPCC is influenced by the stator inductance, stator resistance, and permanent magnet flux linkage. Fig. 16 shows the experimental results of the conventional CCS-MPCC, where the feedback i_q decreases with the decreasing of the stator inductance. Figs. 17 and 18 compare the steady-state performances of the proposed EXM-CCSMPCC and MSET-CCSMPCC under the stator inductance variation. In the whole range of the inductance variation, the i_q keeps the average value of 5 A with both methods. By changing the stator inductance to 9 mH, the i_q of the EXM-CCSMPCC has a large chatter for the later 0.1 s, while that of the MSET-CCSMPCC

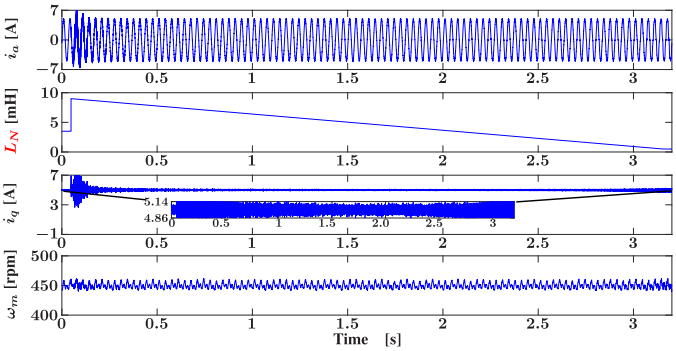

Fig. 17. Steady-state performance under the stator inductance variation. (With the EXM-CCSMPCC, 450 r/min, 5 A i_q).

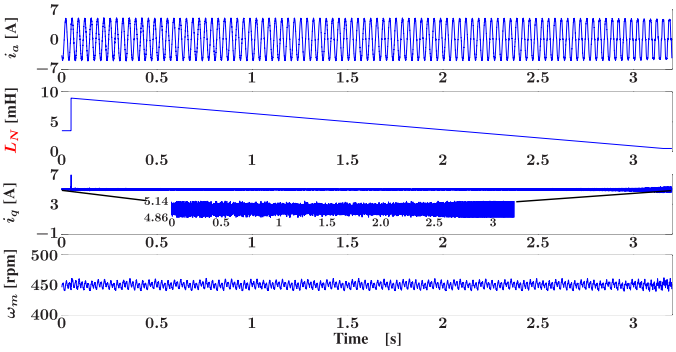

Fig. 18. The steady-state performance under the stator inductance variation. (With the MSET-CCSMPCC, 450 rpm, 5 A i_q).

first jumps to 7 A but returns to 5 A fast. When the stator inductance decreases from 6 to 2.62 mH, the i_q variations of both methods are within 0.28 A. When the inductance decreases from 2.62 to 0.5 mH, the i_q ripples increase, but the i_q ripples of the MSET-CCSMPCC increase more rapidly than that of the EXM-CCSMPCC.

V. Conclusion

This article has proposed a robust CCS-MPC control method for an SPMSM. An extended SPMSM model and a fast terminal sliding mode DO are considered for disturbance compensation. Furthermore, a multistep error tracking CCS-MPCC is proposed to reduce the overshoot while keeping excellent steady-state and dynamic response performances. The major contributions of the proposed strategy include the following.

1) An SMD improved FTSMDO is designed to estimate the lumped disturbances.
2) A multistep error tracking based cost index is proposed to improve the tracking performance of the CCS-MPC.
3) A composite control method combining CCS-MPCC and FTSMDO is developed to enhance the disturbance rejection capability of the PMSM system.

The experimental results implemented on an FPGA-based hardware system verify the effectiveness of the proposed method.

References

[1] J. Yang, W. Chen, S. Li, L. Guo, and Y. Yan, "Disturbance/uncertainty estimation and attenuation techniques in PMSM drives: A survey," *IEEE Trans. Ind. Electron.*, vol. 64, no. 4, pp. 3273–3285, Apr. 2017.

[2] S. A. Odhano, P. Pescetto, H. A. A. Awan, M. Hinkkanen, G. Pellegrino, and R. Bojoi, "Parameter identification and self-commissioning in ac motor drives: A technology status review," *IEEE Trans. Power Electron.*, vol. 34, no. 4, pp. 3603–3614, Apr. 2019.

[3] J. Chen, J. Li, and R. Qu, "Maximum-torque-per-ampere and magnetization-state control of a variable-flux permanent magnet machine," *IEEE Trans. Ind. Electron.*, vol. 65, no. 2, pp. 1158–1169, Feb. 2018.

[4] S.-H. Chang and P.-Y. Chen, "Self-tuning gains of PI controllers for current control in a PMSM," in *Proc. 5th IEEE Conf. Ind. Electron. Appl.*, Jun. 2010, pp. 1282–1286.

[5] A. D. Alexandrou, N. K. Adamopoulos, and A. G. Kladas, "Development of a constant switching frequency deadbeat predictive control technique for field-oriented synchronous permanent-magnet motor drive," *IEEE Trans. Ind. Electron.*, vol. 63, no. 8, pp. 5167–5175, Aug. 2016.

[6] B. Wang, Z. Dong, Y. Yu, G. Wang, and D. Xu, "Static-errorless deadbeat predictive current control using second-order sliding-mode disturbance observer for induction machine drives," *IEEE Trans. Power Electron.*, vol. 33, no. 3, pp. 2395–2403, Mar. 2018.

[7] M. Siami, D. A. Khaburi, M. Rivera, and J. Rodriguez, "An experimental evaluation of predictive current control and predictive torque control for a PMSM fed by a matrix converter," *IEEE Trans. Ind. Electron.*, vol. 64, no. 11, pp. 8459–8471, Nov. 2017.

[8] F. Wang, S. Li, X. Mei, W. Xie, J. Rodriguez, and R. M. Kennel, "Model-based predictive direct control strategies for electrical drives: An experimental evaluation of PTC and PCC methods," *IEEE Trans. Ind. Informat.*, vol. 11, no. 3, pp. 671–681, Jun. 2015.

[9] B.-J. Kang and C.-M. Liaw, "A robust hysteresis current-controlled PWM inverter for linear PMSM driven magnetic suspended positioning system," *IEEE Trans. Ind. Electron.*, vol. 48, no. 5, pp. 956–967, Oct. 2001.

[10] Y. Zhang, L. Huang, D. Xu, J. Liu, and J. Jin, "Performance evaluation of two-vector-based model predictive current control of PMSM drives," *Chin. J. Electr. Eng.*, vol. 4, no. 2, pp. 65–81, Jun. 2018.

[11] B. Stellato, T. Geyer, and P. J. Goulart, "High-speed finite control set model predictive control for power electronics," *IEEE Trans. Power Electron.*, vol. 32, no. 5, pp. 4007–4020, May 2017.

[12] R. Guzman, L. G. de Vicuna, A. Camacho, J. Miret, and J. M. Rey, "Receding-horizon model-predictive control for a three-phase VSI with an LCL filter," *IEEE Trans. Ind. Electron.*, vol. 66, no. 9, pp. 6671–6680, Sep. 2019.

[13] A. A. Ahmed, B. K. Koh, and Y. I. Lee, "A comparison of finite control set and continuous control set model predictive control schemes for speed control of induction motors," *IEEE Trans. Ind. Informat.*, vol. 14, no. 4, pp. 1334–1346, Apr. 2018.

[14] M. Zou, S. Wang, M. Liu, and K. Chen, "Model predictive control of permanent-magnet synchronous motor with disturbance observer," in *Proc. IEEE Int. Symp. Predictive Control Electr. Drives Power Electron.*, May 2019, pp. 1–6.

[15] J. Wang, S. Li, J. Yang, B. Wu, and Q. Li, "Finite-time disturbance observer based non-singular terminal sliding-mode control for pulse width modulation based DC-DC buck converters with mismatched load disturbances," *IET Power Electron.*, vol. 9, no. 9, pp. 1995–2002, 2016.

[16] B. Wang, X. Chen, Y. Yu, G. Wang, and D. Xu, "Robust predictive current control with online disturbance estimation for induction machine drives," *IEEE Trans. Power Electron.*, vol. 32, no. 6, pp. 4663–4674, Jun. 2017.

[17] S. Lin, Y. Cai, B. Yang, and W. Zhang, "Electrical line-shafting control for motor speed synchronisation using sliding mode controller and disturbance observer," *IET Control Theory Appl.*, vol. 11, no. 2, pp. 205–212, 2017.

[18] X. Zhang, L. Sun, K. Zhao, and L. Sun, "Nonlinear speed control for PMSM system using sliding-mode control and disturbance compensation techniques," *IEEE Trans. Power Electron.*, vol. 28, no. 3, pp. 1358–1365, Mar. 2013.

[19] X. Zhang, B. Hou, and Y. Mei, "Deadbeat predictive current control of permanent-magnet synchronous motors with stator current and disturbance observer," *IEEE Trans. Power Electron.*, vol. 32, no. 5, pp. 3818–3834, May 2017.

[20] Y. Jiang, W. Xu, C. Mu, and Y. Liu, "Improved deadbeat predictive current control combined sliding mode strategy for PMSM drive system," *IEEE Trans. Veh. Technol.*, vol. 67, no. 1, pp. 251–263, Jan. 2018.

[21] Y. Feng, X. Yu, and F. Han, "High-order terminal sliding-mode observer for parameter estimation of a permanent-magnet synchronous motor," *IEEE Trans. Ind. Electron.*, vol. 60, no. 10, pp. 4272–4280, Oct. 2013.

[22] S. Yu, X. Yu, and R. Stonier, "Continuous finite-time control for robotic manipulators with terminal sliding modes," in *Proc. 6th Int. Conf. Inf. Fusion*, Jul. 2003, vol. 2, pp. 1433–1440.
[23] L. Fridman and A. Levant, "High order sliding modes as the natural phenomenon in control theory," in *Robust Control via Variable Structure and Lyapunov Techniques*, vol. 217, F. Garofalo and L. Glielmo, Eds., Berlin, Germany: Springer-Verlag, Jan. 1996, pp. 107–133.
[24] J. Han, "From PID to active disturbance rejection control," *IEEE Trans. Ind. Electron.*, vol. 56, no. 3, pp. 900–906, Mar. 2009.
[25] M. Iqbal, A. I. Bhatti, S. I. Ayubi, and Q. Khan, "Robust parameter estimation of nonlinear systems using sliding-mode differentiator observer," *IEEE Trans. Ind. Electron.*, vol. 58, no. 2, pp. 680–689, Feb. 2011.

Fengxiang Wang (Senior Member, IEEE) was born in Jiujiang, China, in 1982. He received the B.S. degree in electronic engineering and the M.S. degree in automation from Nanchang Hangkong University, Nanchang, China, in 2005 and 2008, respectively, and the Ph.D. degree from the Institute for Electrical Drive Systems and Power Electronics, Technische Universitaet Muenchen, Munich, Germany, in 2014.

He is currently a Full Professor and Deputy Director of Quanzhou Institute of Equipment Manufacturing, Haixi Institutes, Chinese Academy of Sciences, Beijing, China.

Dr. Wang serves as an IET fellow, and as an Associate Editor for the IEEE TRANSACTIONS ON INDUSTRIAL ELECTRONICS and IEEE TRANSACTIONS ON ENERGY CONVERSION. As the General Chair, he organized the IEEE 5th International Symposium on Predictive Control of Electrical Drives and Power Electronics.

His research interests include predictive control and sensorless control for electrical drives and power electronics.

Long He (Member, IEEE) was born in Fuzhou, China, in 1984. He received the B.S. degree in applied physics and the M.S. degree in physical electronics from Fuzhou University, Fuzhou, China, in 2007 and 2010, respectively.

He is currently working with Haixi Institutes, Chinese Academy of Sciences, Beijing, China. His research interests include predictive control and sensorless control for electrical drives.

Jose Rodriguez (Fellow Member, IEEE) received the Engineer's degree from the Universidad Tecnica Federico Santa Maria, Valparaiso, Chile, in 1977, and the Dr.-Ing. degree from the University of Erlangen, Erlangen, Germany, in 1985, both in electrical engineering.

Since 1977, he has been with the Department of Electronics Engineering, Universidad Tecnica Federico Santa Maria, where he was a full Professor and President. Since 2015, he has been the President of Universidad Andres Bello in Santiago, Chile. He has coauthored two books, several book chapters, and more than 400 journal and conference papers. His main research interests include multilevel inverters, new converter topologies, control of power converters, and adjustable-speed drives.

Dr. Rodriguez has received a number of best paper awards from journals of the IEEE. He is a member of the Chilean Academy of Engineering. In 2014, he received the National Award of Applied Sciences and Technology from the Government of Chile. In 2015, he received the Eugene Mittelmann Award from the IEEE Industrial Electronics Society.